

Elevated Temperature Deformation of Cast Inconel 718

Luis Mendoza Camus* and Goran Engberg**

* *Royal Institute of Technology, Stockholm, Sweden.*

** *SSAB Strip Products Ltd., Borlänge, Sweden*

CONTENTS

	Page
ABSTRACT	28
1. INTRODUCTION	28
2. EXPERIMENTAL	29
3. RESULTS	30
3.1. As cast material	30
3.2. Coarsening behaviour of γ' and γ'' particles	31
3.3. Tensile tests	33
4. CONCLUSIONS	37
ACKNOWLEDGEMENTS	38
REFERENCES	38

ABSTRACT

The rate of coarsening of γ' and γ'' particles was evaluated for Inconel 718. The elevated temperature deformation behaviour was studied through tensile tests at 430, 550 and 650°C combined with TEM studies of deformed structures. The coarsening kinetics for both γ' and γ'' type particles are in good agreement with the LSW theory within the temperature range 550 to 750°C.

Dynamic strain ageing contribute strongly to the deformation behaviour specially at 650°C but also at 430 and 550°C.

The Bailey Orowan type of relation for dislocation slip and recovery provides an excellent means of describing the stress-strain behaviour when coupled with a model for the locking effect of diffusing elements to the dislocations. In spite of the simplifying assumption used the model gives a very good description of the experimental data for all conditions of testing. The dominating mechanism of particle strengthening is most probably a combination of APB cutting with the first dislocation in the pair completely flexible and as a consequence also coupled with some bypassing by the Orowan mechanism.

1. INTRODUCTION

The flow stress, σ , is related to the total dislocation density, ρ , in a crystalline material by

$$\sigma = \sigma_0 + m\alpha Gbp^{1/2} \quad (1)$$

σ_0 equals all other athermal and thermal parts of the flow stress, we will adopt the designation friction stress for this parameter hereafter. m is the Taylor factor, α the strength of the dislocation interaction barriers, G the shear modulus and b Burgers' vector. If deformation is dominated by dislocation slip we may write

$$\frac{d\rho}{dt} = \frac{m}{bL} \frac{d\varepsilon_p}{dt} - M\rho^2 \quad (2)$$

where L is the mean free distance for dislocation slip and M is the rate constant for dislocation recovery (by climb and/or cross-slip). M is given by 1/

$$M = - \frac{2D_S b^3 G}{kT \ln(bp^{1/2})} \quad (3)$$

where D_S is the coefficient for self diffusion, k the Boltzmann constant and T the absolute temperature.

The mean free distance of slip is considered to be either a constant, independent of strain, or dependent upon strain through the interdislocation spacing,

$$L = a, \quad \text{or} \quad (4a)$$

$$L = \frac{b}{\rho^{1/2}} \quad (4b)$$

where b is a constant close to 1. During a tensile test we further have,

$$\frac{d\varepsilon_{\text{tot}}}{dt} = \frac{d\varepsilon_{\text{pl}}}{dt} + \frac{1}{E} \frac{d\sigma}{dt} \quad (5)$$

where E is Youngs' modulus (or the stiffness of the tensile system used).

The situation is complicated if dynamic strain ageing occurs. A fairly straight forward way of dealing with this phenomenon is to assume that dislocations get locked, prevented from slip or restricted from recovery, when a certain saturation of the diffusing species is reached at the dislocations. We may thus describe the degree of locking, p , by the saturation per unit length of a dislocation,

$$p = \frac{k_1}{\bar{\rho}} e^{-\frac{k_2 Q_{\text{sol}}}{T}} (1 - e^{-\frac{k_3 \rho (D_S G b^3)^{2/3}}{T}}) \quad (6)$$

with $p \leq 1$

We have put all parameters without temperature dependence in the three constants, k . Q_{sol} describes the temperature dependence of the solubility in the usual way. The locking effect will be independent of the dislocation density for low densities and will be insignificant for large densities as soft impingement becomes important. The change in the locked dislocation density, ρ_1 , with time can be written as

$$\frac{d\rho_1}{dt} = p \frac{d\rho}{dt} \quad (7)$$

where ρ_1 is the free dislocation density. The total dislocation density is given by the sum of the locked and the free density. By differentiating equation 1 with time and combining with equations 2, 5 and 7 we obtain

$$\frac{d\sigma}{d\varepsilon_{\text{tot}}} = \frac{(1 - \frac{MbL(1-p)^2(\sigma-\sigma_0)^4}{m(m\alpha Gb)^4 \frac{d\varepsilon_{\text{tot}}}{dt}})}{(\frac{2bL(1-p)(\sigma-\sigma_0)}{m(m\alpha Gb)^2} + \frac{1}{E})} \quad (8)$$

We have made a not quite stringent simplification when deriving equation 8 since we have substituted the absolute value of the free dislocation density with $(1-p)$ times the total dislocation density while this is true only for the differentials. Otherwise we have assumed that it is only the free dislocations that contribute to slip and recovery while the total density gives the strength of the material. We have further assumed that the mean free distance of slip is independent of strain.

The particle strengthening contribution in the present kind of alloy depends in a rather complex manner on volume fractions and particles sizes of the two main types of particles, γ' and γ'' . In a recent review [2] four different mechanisms are

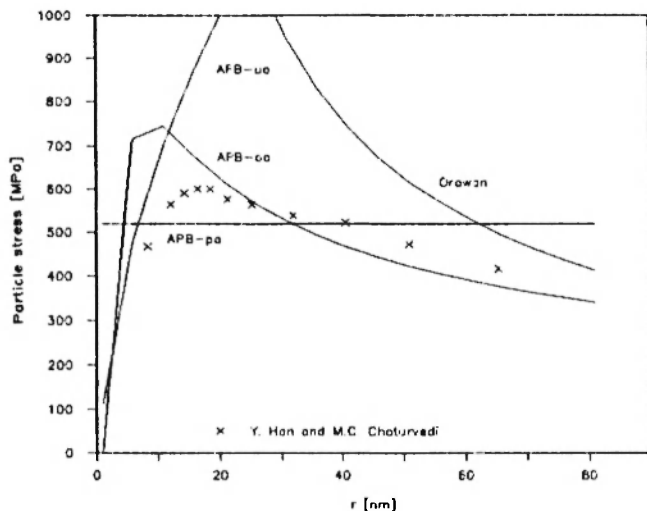


Fig. 1 Calculated strengthening contribution from γ' and γ'' particles at 600°C. APB-ua, -pa and -oa stands for under-aged, peak-aged and over-aged (see text).

listed. Three of these treat particle cutting assuming that the particle strength is given by the creation of anti-phase boundaries (APB). For these cases the dislocations are assumed to interact pairwise with the particles. The differences stem from different configurations of the two dislocations depending on particle dispersion. The fourth mechanism is the Orowan process. Assuming volume fraction and particle size to be constant during the test the only temperature dependent terms in the relations for the four mechanisms are the APB energy and the shear modulus.

In Fig. 1 the variation in the strengthening contribution has been calculated assuming reasonable values for the different parameters.

γ' : APB-energy = 0.000296 N/mm
Volume fraction = 14.25%

γ'' : APB-energy = 0.000175 N/mm
Volume fraction = 4.75%

Young's modulus = 78900*(1-0.64*T(°C)/1723),
(ref. [3])

Burger's vector = 0.25 nm

Taylor's factor = 3.1

In the figure we have also included experimental results from creep tests where the particle strengthening contribution has been evaluated by the consecutive stress reduction method [4]. As can be seen, a very good agreement between theory and experiments is obtained.

2. EXPERIMENTAL

Specimens of Inconel alloy 718, with chemical composition according to Table 1, were subjected to the conventional heat treatment (cht) for this cast alloy.

Table 1. Chemical composition in weight-%.

Ni	Fe	Cr	Ti	Mo	Nb	Al	Ta	Co	Mn
53.3	17.58	18.83	0.98	2.97	5.13	0.53	0.05	0.30	0.09
C	S	P	Si	Cu					
0.04	0.004	0.01	0.17	0.09					

Cht consists of solution treatment at 954°C for 1 hr. followed by aircooling to 760°C, where the material is kept for 5 hrs. The material is then cooled to 650°C at a cooling rate of 55°C/hr. It is then kept for 1 hr. at 650°C and finally air cooled to room temperature.

Tensile tests were performed in a 100 kN mechanical tensile test machine (Instron). The test temperatures were 430, 550 and 650°C. At each temperature three initial strain rates were used; 1.33×10^{-2} , 10^{-4} and 6.6×10^{-6} per second. The temperature was monitored by three spotwelded type S thermocouples on each specimen.

A second series of tensile tests were performed at 430, 550 and 650°C at a strain rate of 6.6×10^{-6} . The tests were interrupted after a plastic strain of 0.3 or 0.6%. The structures were to some degree quenched in by using pressurized air for "fast" cooling from the test temperature. Thin foils were manufactured and particle and dislocation structures were studied in a 200 kV Jeol transmission electron microscope. The foils were prepared by jet electropolishing 3 mm diameter discs in 15% perchloric acid, 85% methanol at -15°C and 30V.

In order to quantify particle coarsening a series of ageing treatments was performed according to the matrix shown in Table 2.

Table 2. Ageing treatments.

Temperature (°C)	Time (hours)			
	125	1000	3375	8000
550	125	1000	3375	8000
650	16	125	420	1000
750	2	16	125	420

The particle sizes were determined from TEM micrographs of thin foils obtained as above.

The microstructure of the alloy prior to ageing treatments was studied using light optical microscopy. The specimens were prepared by mechanical polishing and electroetching using glyceria (containing 5 ml HNO₃, 10 ml HCL and 15 ml glycerin). The study was also performed in order to ensure microstructural homogeneity of the cast material, see cross section in Fig. 2, from which tensile specimens and samples for ageing studies were obtained. Microhardness measurements were performed across dendrites.

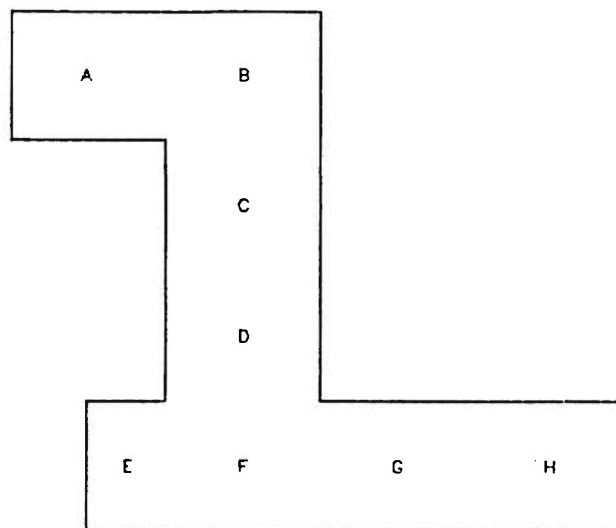


Fig. 2 Schematic view of cross-section of cast material. The letters refer to different specimen locations.

3. RESULTS

3.1 As Cast Material

The microstructure is fairly complex. A low magnification picture is given in Fig. 3. In the interdendritic areas several different phases exist, Fig. 4.

The intragranular platelets (Widmanstätten morphology) are associated with precipitation of η (stable, hexagonal Ni₃Ti) [5]. This phase is believed to be the result of a transformation of metastable fcc Ni₃Ti (γ') at elevated temperatures during forming or heat treatment [6]. The randomly oriented, globular phase at the grain boundaries,



Fig. 3 Microstructure in the as-cast condition.

Fig. 3, is probably the stable, orthorhombic Ni_3Nb (δ) phase which, in turn, is believed to form from the metastable, ordered, bct γ'' phase at elevated temperature. Carbide, MC with Cr, is found in the interdendritic regions.

The microhardness measurements revealed no significant variation between samples from different locations (B, D, H and F in Fig. 1) in the cast component. The difference between the middle of the dendrites and the interdendritic areas was approximately 160 HV (100g), with the highest hardness in the interdendritic areas.

Energy dispersive analysis was performed across the dendrites and the results are summarized in Table 3. Segregation of Nb, Ti and Al in the interdendritic areas is evident.

Table 3. EDS measurements of concentration in dendritic and interdendritic areas. As-cast microstructure.

Location	Fe	Ni	Cr	Nb	Ti	Mo	Al	Co
Inter-dendritic	19.6	53.0	19.5	5.1	0.99	3.4	0.67	0.35
dendritic	17.4	51.1	17.6	3.5	0.74	2.6	0.40	0.04

3.2 Coarsening Behaviour of γ' and γ'' Particles

The high density of precipitates and the coherency strains associated with the particles makes size measurements impossible in bright field TEM micrographs, Fig. 5. The identification of the two different types of particles is also impossible. Using dark field micrographs from superlattice reflections in [001] diffraction patterns the phases can be identified and their respective sizes measured, Figs. 6 to 8. The superlattice reflections have been indexed with respect to the fcc matrix. Reflections of the type [11/20] are permitted in the DO_{22} bct (γ'') phase but not in the fcc (γ') or the orthorhombic Ni_3Nb phases.

The bct γ'' precipitates can grow with the c axis along any of the three $\langle 001 \rangle$ directions in the matrix. In the indexing system chosen for the electron diffraction pattern, conversion from $(hkl)_{\text{fcc}}$ to $(hkl)_{\text{bct}}$ is accomplished by doubling the fcc index corresponding to the c axis. The allowed reflections for the bct γ'' phase are given by $(h+k+l)=2n$, where n is an integer. Accordingly, the

reflection indexed [11/20] in Fig. 6 can only have been produced by the [010] variant of the bct γ'' phase. On the other hand the [100] reflection is allowed for both γ' and [100] γ' variant, but not for the [010] and [001] variants of γ'' . The streaking of the superlattice reflections (Fig. 6) suggests that bct γ'' has a disc-shape with the c-axis perpendicular to the plane of the disc.

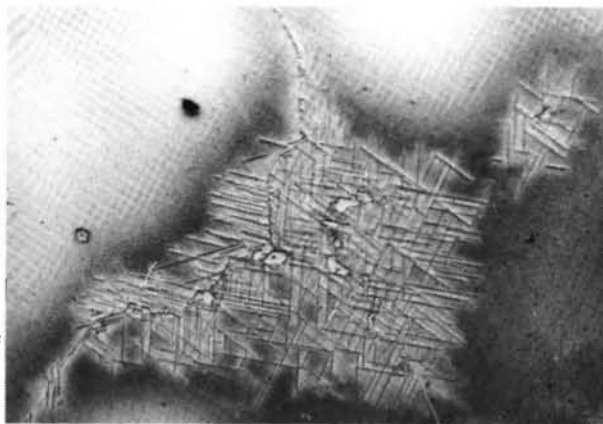


Fig. 4 Widmanstätten like precipitates, probably $\eta\text{Ni}_3\text{Ti}$, and globular grain boundary phase, probably $\delta\text{Ni}_3\text{Nb}$.

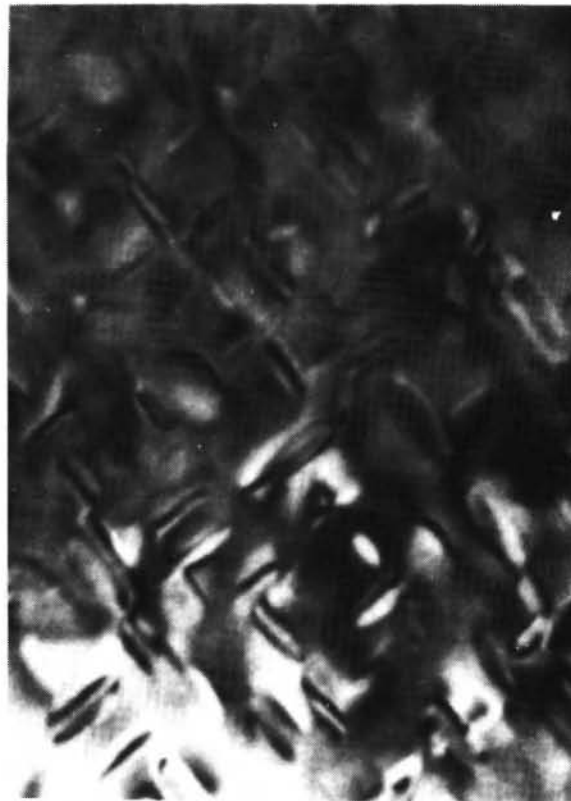


Fig. 5 Bright field micrograph. Chl. Magnification 375000 x.

In Fig. 7 two variants of γ'' in the same area of one foil are shown. In Fig. 8, γ'' and γ'' plus γ' are shown in a) and b), respectively. Due to the comparatively low volume fraction of γ' particles their occurrence is sparse and the main part of the particles observed are γ'' . The determination of the size of γ' was not always possible due to this fact. Table 4 contains the size of the particles after the different ageing times.

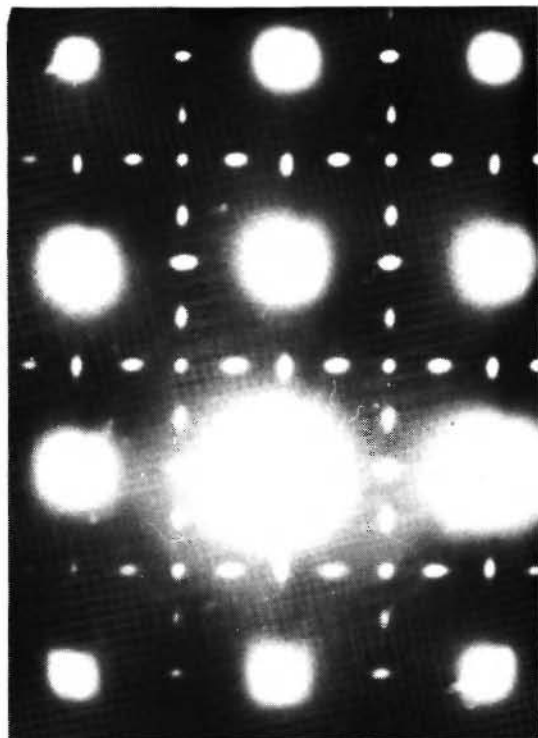


Fig. 6 Diffraction pattern. Zone axis [001].

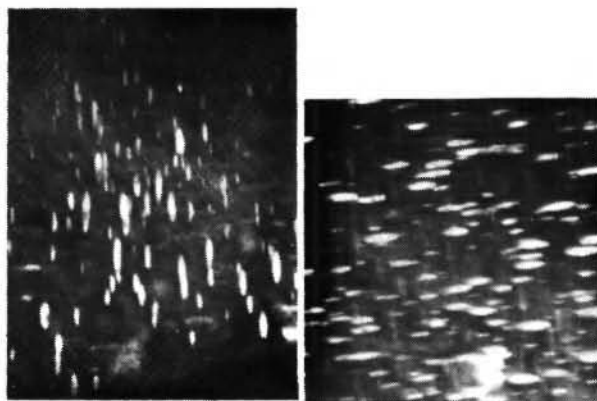


Fig. 7 Cht plus ageing for 125 hr. at 650°C. Magnification 125000 x.
a. [1/210] variant of γ'' .
b. [11/20] variant of γ'' .



Fig. 8 Cht plus ageing for 450 hr. at 750°C. Magnification 50000 x.
a. [1/210] variant of γ'' .
b. [1/210] variant of γ'' and γ' .

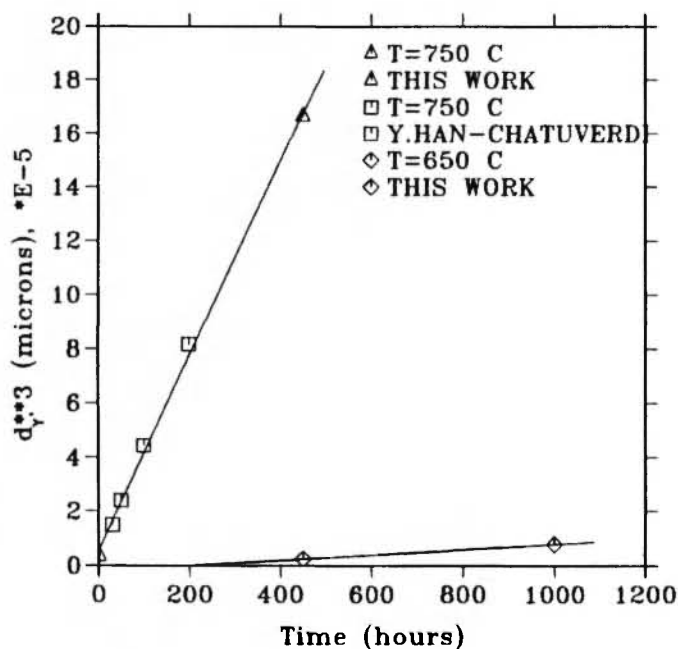


Fig. 9 Variation in γ' (diameter)³ with ageing time at different ageing temperatures.

$$d^3 - d_0^3 = K \frac{\gamma^p q D_S C_e V_m^2}{RT} t \quad (9a)$$

or simplified

$$d^3 - d_0^3 = K' \frac{e^{-\frac{Q_c}{RT}}}{T} t = K'' t \quad (9b)$$

where d is the mean (major) diameter, q is the aspect ratio ($=d/h$ where h is the thickness) and K , K' , K'' are constants, V_m is the molar volume, γ^p the particle/matrix interphase energy, C_e the equilibrium concentration of the diffusing species and D_S their diffusion coefficient. Q_c is the activation energy for the process (including contributions from D_S and C_e). In the derivation of the activation energy we used our data plus the data of Han et al [7]. The activation energies obtained are 285000 J/mol and 300000 J/mol for γ'' and γ' , respectively. These values are close to the activation energy for diffusion of Ti and Al in Ni, 257000 and 270000 J/mol, respectively, [8]. The activation energy for diffusion of Nb in Ni-Fe-Nb alloys is 264000 J/mol [9]. The rates of coarsening are given in equation 10.

$$\begin{aligned} \gamma'': \quad d^3 &= (416)^3 \\ &= \frac{1.410 \cdot 10^{20} q e^{-\frac{285000}{RT}}}{T} t \end{aligned} \quad (10a)$$

$$\begin{aligned} \gamma': \quad d^3 &= (120)^3 \\ &= \frac{2.610 \cdot 10^{20} q e^{-\frac{300000}{RT}}}{T} t \end{aligned} \quad (10b)$$

The diameters are expressed in Angstrom units and the time in seconds. The values for the initial diameters are mean values for all tests.

3.3 Tensile Tests

The stress-plastic strain curves are given in Fig. 11. As is seen, a negative strain-rate dependence is obtained at the highest temperature and, to some extent, also at the lower temperatures. In order to analyze the curves numerical differentiation was performed and $d\epsilon_{10\%}/d\sigma$ was

TABLE 4

Experimentally obtained particles sizes.
 d and h for γ'' denotes the diameter
and the thickness of the disc, respectively.

T	time	γ''			γ'
(K)	(hr)	$d(\text{\AA})$	$h(\text{\AA})$	$q(d/h)$	$d(\text{\AA})$
823	125	384	92	4.2	--
	1000	384	98	3.9	--
	3400	387	49	7.9	--
	8000	432	105	4.1	--
923	16	250	41	6.1	--
	125	436	79	5.5	--
	450	412	96	4.3	135
	1000	620	106	5.9	199
1023	2	324	63	5.1	150
	16	552	97	5.7	--
	125	1389	276	5.0	--
	450	1942	253	7.7	631

evaluated. The data were then fitted to equation 8. The friction stress was assumed to be directly proportional to the shear modulus. Ignoring the effects of recovery (putting M equal to zero) and of dynamic strain ageing (p equal to zero), the behaviour at the highest strain rate was well described if the mean free distance of slip was put equal to 0.025 mm and the friction stress was equal to 0.0128 times the shear modulus, Fig. 12. The constants in the expressions for p and a correction factor for M were then determined by manual fitting

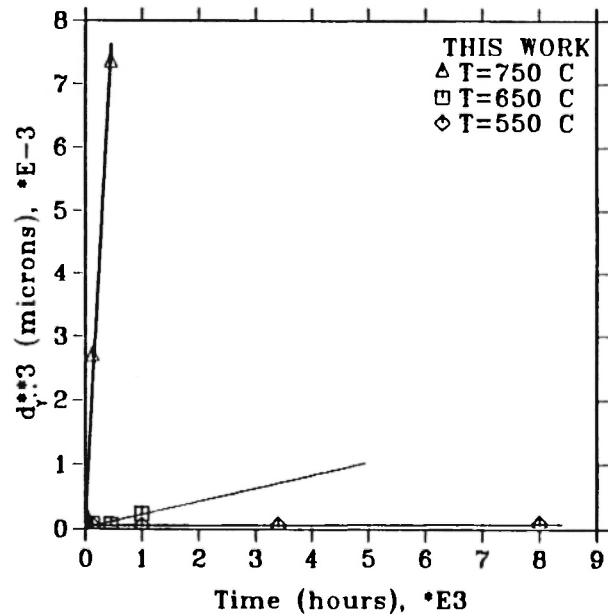


Fig. 10 Variation in γ'' (diameter)³ with ageing time at different ageing temperatures.

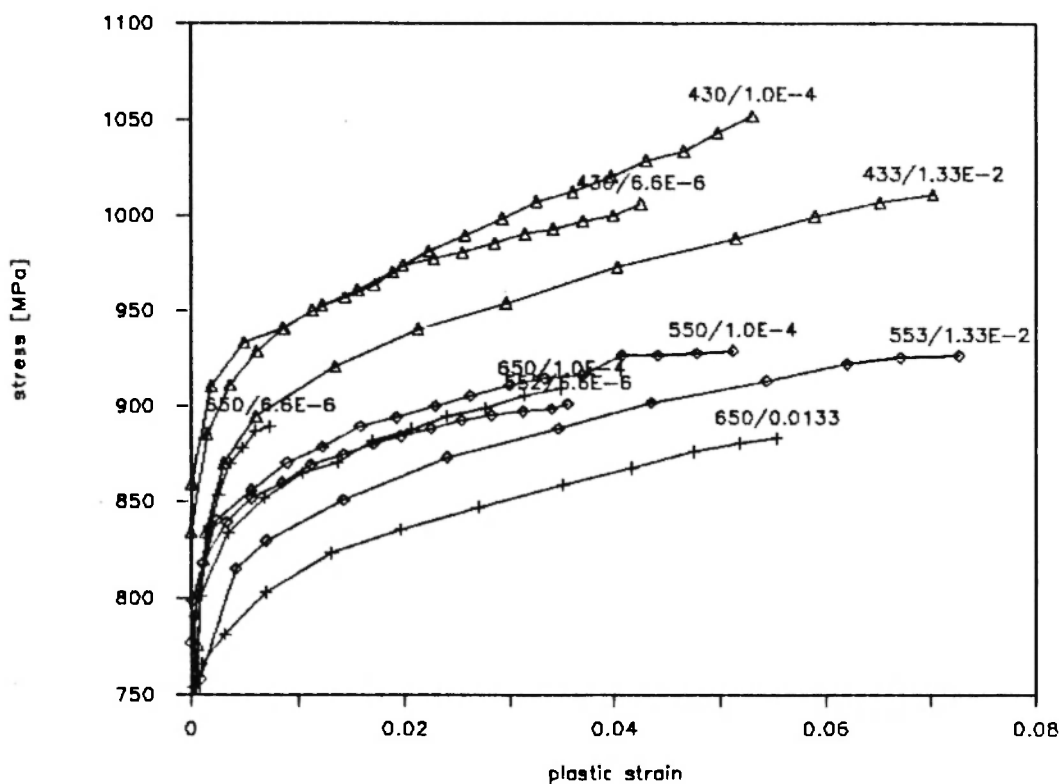


Fig. 11 Stress versus plastic strain for all tests performed. The values at the curves denote temperature (°C) and strain-rate (1/s) for the tests.

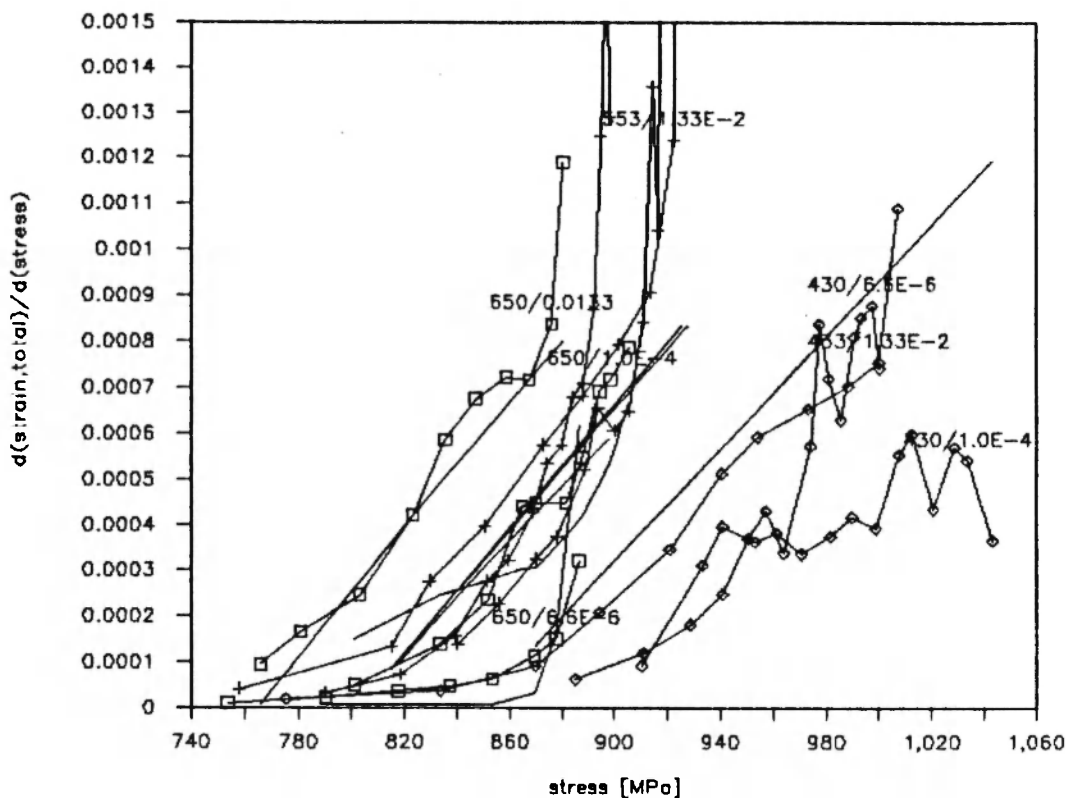


Fig. 12 Analysis of the stress-strain curves using equation 8.

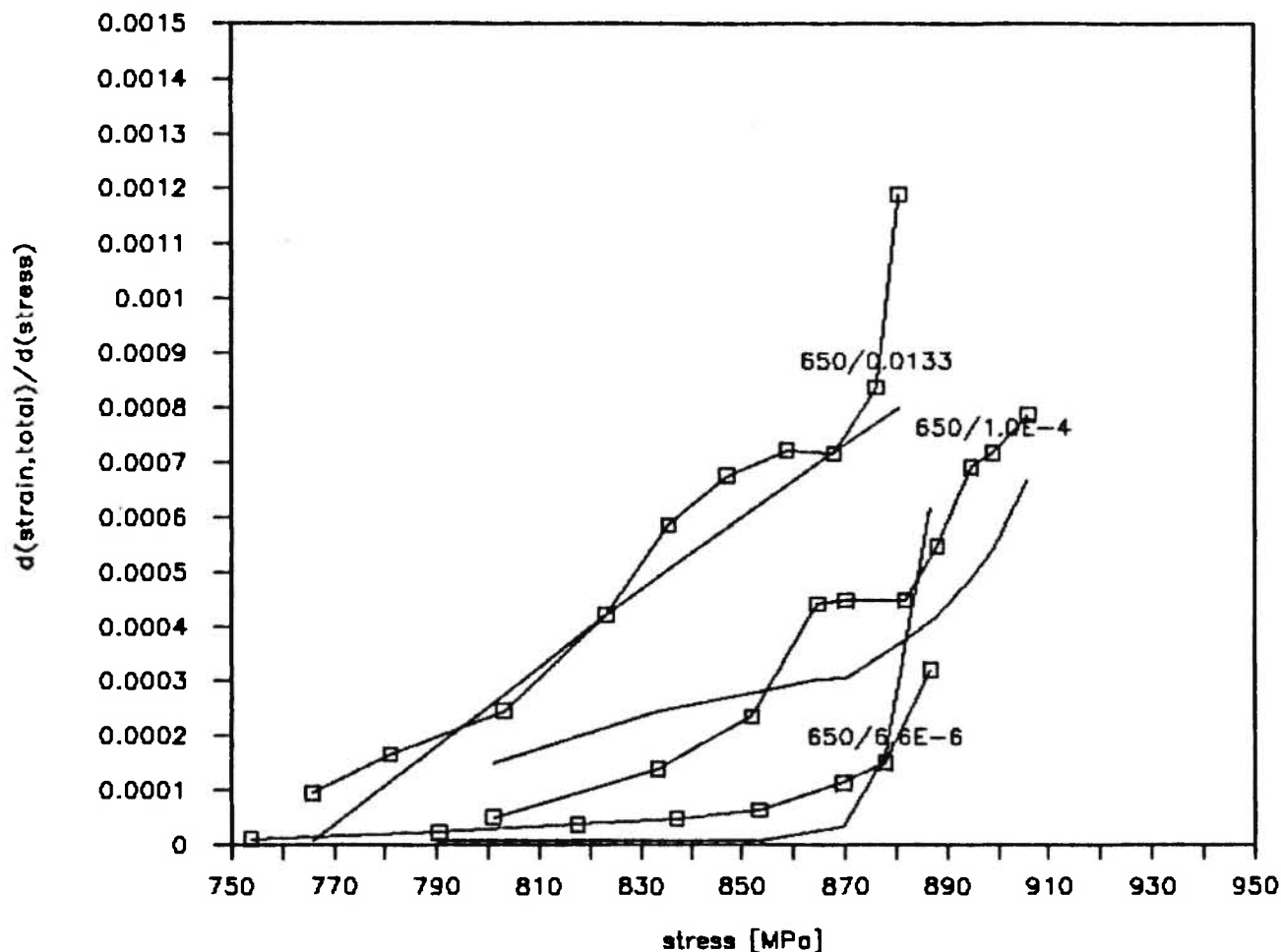


Fig. 13 Analysis of the stress-strain curves at 650°C using equation 8.

of the calculated curves to the experimentally observed ones. In Fig. 13 the results for the highest temperature are displayed. A fairly good description of the actual behaviour is obtained in spite of all the simplifications. The values for the constants used are given in Table 5.

The rest of the parameters used have been stated in the text above. Only five parameters have been fitted and their values seem quite reasonable.

The experimentally obtained values of the friction stress are higher than the values given in Fig. 1. The calculations giving the values in Fig. 1 assumed APB strengthening to be the only contribution. The transmission electron micrographs (Fig. 5) show that the particles have a considerable associated strain field. We should thus expect coherency strains to contribute. We also have contributions from grain boundaries etc.

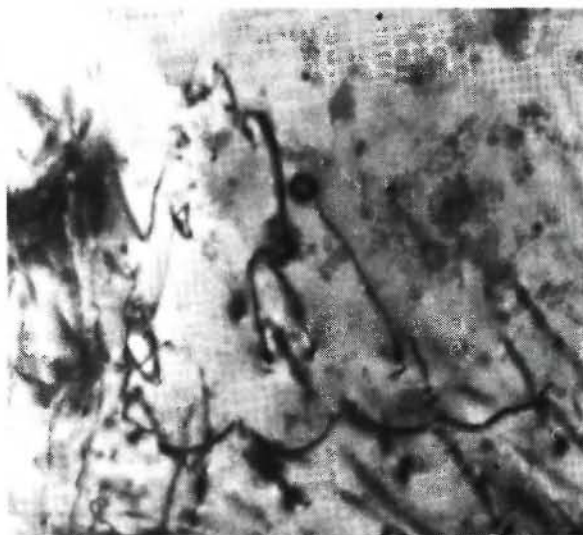


Fig. 14 Deformation temperature, 430°C. After 0.6% plastic deformation.

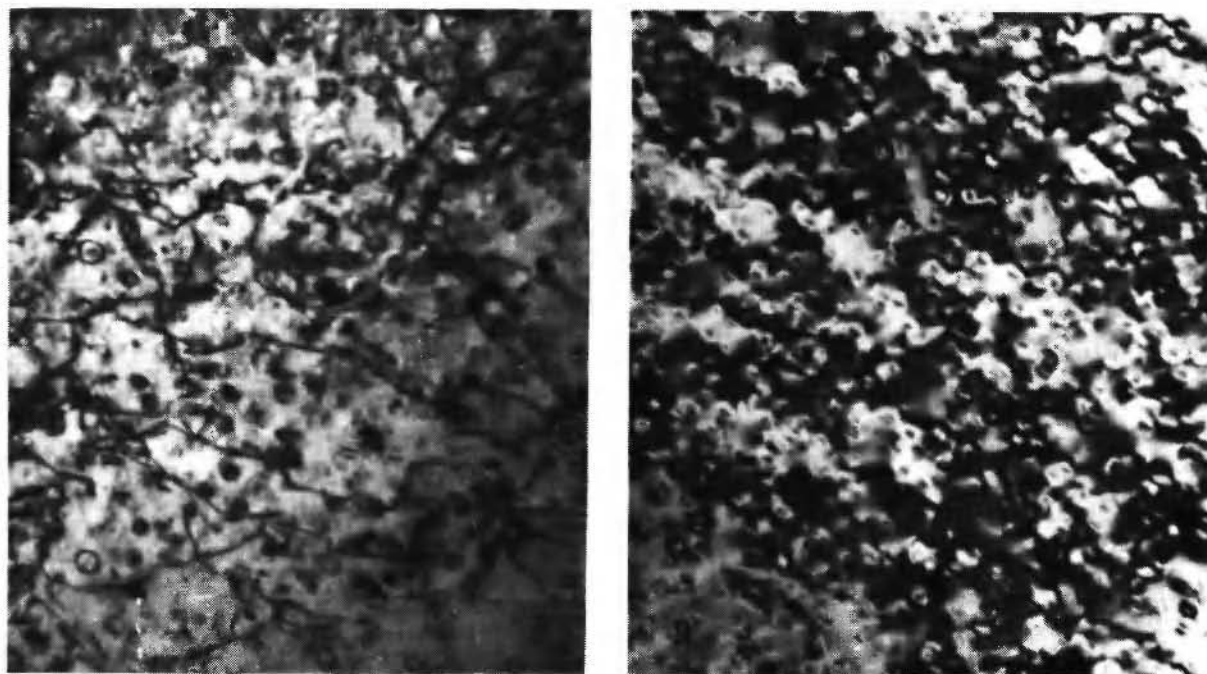


Fig. 15 Deformation temperature, 550°C.

a) after 0.3% plastic deformation.

b) after 0.6% plastic deformation.

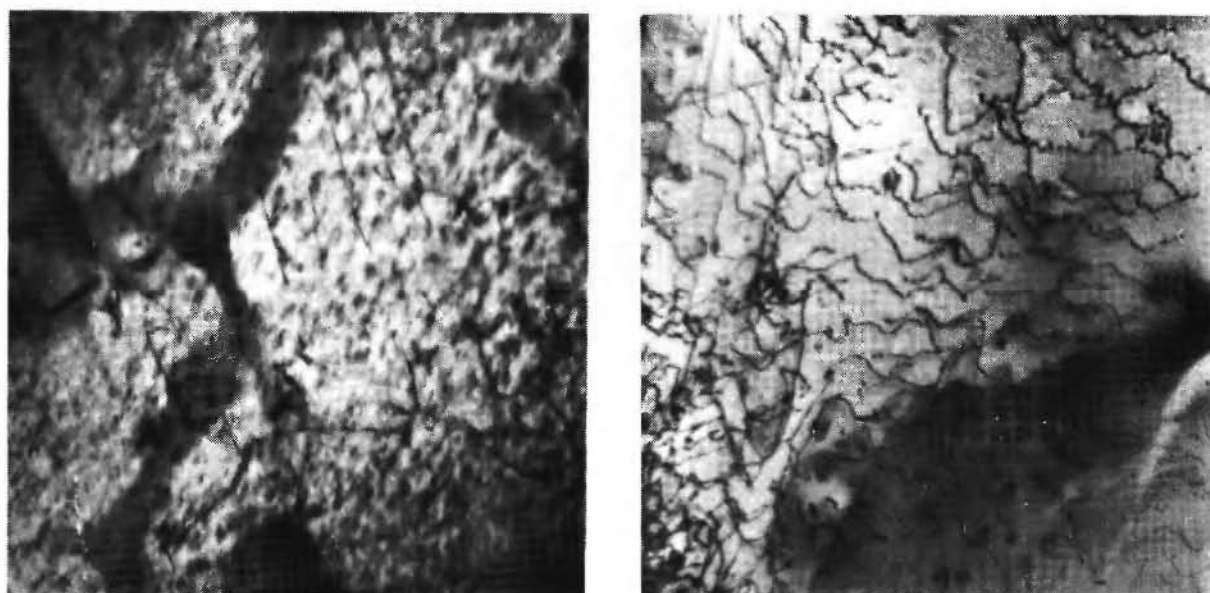


Fig. 16 Deformation temperature, 650°C.

a) after 0.3% plastic deformation.

b) after 0.6% plastic deformation.

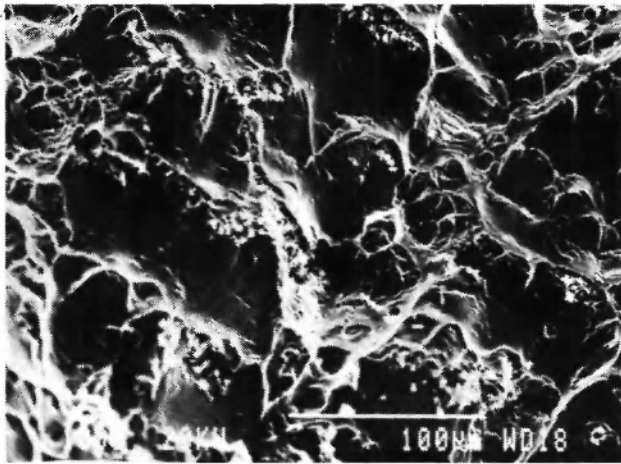


Fig. 17 Fracture surface of the specimen deformed at 650°C at a strain rate of $6.6 \cdot 10^{-6}$ 1/s.

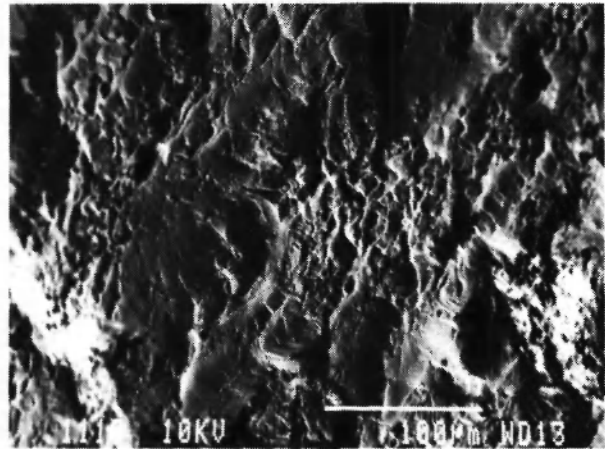


Fig. 18 Fracture surface of the specimen deformed at 650°C at a strain rate of $1.3 \cdot 10^{-2}$ 1/s.

Tensile tests performed at 430, 550 and 650°C and at the lowest strain-rate ($6.6 \cdot 10^{-6}$ 1/s) were interrupted after plastic strains of 0.3 and 0.6%. Sections were then cut from these specimens and thin foils for TEM manufactured. The dislocation structures consisted mainly of single dislocations and loops around particles. In some cases dislocations arranged pairwise were discerned. The structures, which are shown in Figs. 15 and 16, were quite similar irrespective of temperature of testing. In Fig. 16 many of the dislocations seem to be locked on a finer scale than the particles warrant. The number of loops is less at this temperature, 650°C, than at the other. This is probably due to annealing out of the loops and the locking effect may be due to strain ageing.

The particle sizes after chf were measured. The mean diameter for γ' was 176 Å and for γ'' we found a mean diameter of 283 Å and a mean thickness of 70 Å (aspect ratio 4.0). The equivalent radius (for a sphere with the same volume as the disc) is approximately 80 Å. Inspection of Fig. 1 reveals that this would correspond to particle cutting with the first dislocation completely flexible. With this mechanism we also expect the Orowan mechanism to be present in the sense that loops are left behind the

moving dislocations in some cases and in others cutting takes place. The conclusion is that experiment and theory are in reasonable agreement.

The fracture surfaces revealed a significant difference between the appearance of the specimen tested at 650°C at a strain rate of $6.6 \cdot 10^{-6}$ 1/s and all the rest. The former, Fig. 17, displayed large amounts of coarse second phase particles in the fracture surface in contrast to the other specimens, Fig. 18. The surface of the former also showed a smaller number of dimples than the rest and the surface had a dendrite like appearance. The low strain rate at the comparatively high temperature, together with dynamic strain ageing, obviously favoured grain boundary deformation mechanisms leading to intercrystalline fracture.

4. CONCLUSIONS

The coarsening kinetics for both γ' and γ'' type particles are in good agreement with the LSW theory within the temperature range 550 to 750°C.

Dynamic strain ageing contributes strongly to the deformation behaviour, especially at 650°C but also at 430 and 550°C.

The Bailey Orowan type of relation for dislocation slip and recovery provides an excellent means of describing the stress-strain behaviour when coupled with a model for the locking effect of diffusing elements to the dislocations. In spite of the simplifying assumptions used, the model provides a very good description of the experimental data for all conditions of testing.

The dominating mechanism of particle strengthening is most probably a combination of APB cutting with the first dislocation in the pair completely flexible and, as a consequence, also coupled with some bypassing by the Orowan mechanism.

ACKNOWLEDGMENTS

The authors wish to thank Dr. B. Bergman for valuable suggestions concerning the TEM studies and N. Lange for his help in the experimental part of this work.

REFERENCES

1. ENGBERG, G., TRITA-MAC-0098, Materials Center, RIT Stockholm, 1976.
2. NEMBACH, E. and NEITE, G., *Progress in Mater. Sci.* **29**, 177-319 (1985).
3. FROST, H.J. and ASHBY, M.F., **Deformation mechanism maps**. Pergamon Press, Oxford, 1982.
4. HAN, Y. and CHATURVEDI, M.C., *Mater. Sci. Eng.* **85**, 59-65 (1987).
5. KOHLHAAS, E. and FISHER, A., **The metallography of superalloys**. Special issue (2), App. Electron Metallography, Practical Metallography, p. 125, 1970.
6. BROWN, E.E. and MUZYKA, D.R., **Superalloy 2**. Ed. Sims, Stoloff and Hagel, Wiley Intersci. Publ., USA, 1987.
7. HAN, Y., DEB, P. and CHATURVEDI, M.C., *Metal Sci.* **16**, 555-561 (1982).
8. **Diffusion Data J.**, **17**, 62, (1978).
9. **Diffusion Data J.**, **6**, 352, (1972).